Journal of Materials Chemistry B

Accepted Manuscript

ROYAL SOCIETY OF CHEMISTRY

www.rsc.org/materialsB

Facile Preparation of Graphene Nanoribbon/Cobalt Coordination Polymer Nanohybrid for Non-enzymatic H_2O_2 Sensing by Dual Transducer: Electrochemical as well as Fluorescence

Sanjeev K. Ujjain[a,b*], Preety Ahuja[b], Raj Kishore Sharma[b*]

[a]Department of Physics, Indian Institute of Technology Kanpur, Kanpur, UP-208016, India.

[b]Department of Chemistry, University of Delhi, Delhi-110007, India.

ABSTRACT

A novel graphene nanoribbon (GNR)/cobalt coordination polymer (MCPs) composite (MCPs@GNR) is prepared by in-situ reduction of graphene oxide nanoribbon (GONR) with simultaneous growth of MCPs nanoparticles on its surface. Morphology and structure are investigated by High Resolution Transmission Electron Microscope (HRTEM), Scanning electron microscopy (SEM), UV-Vis, X-Ray photoelectron spectroscopy (XPS), Fourier transform-infrared spectroscopy, X-ray diffraction and Raman spectroscopy. Results indicate that MCPs nanoparticles having dia. ~6 nm are successfully deposited on GNR to form a hybrid conducting network. Analytical performance of the MCPs@GNR composite shows high non-enzymatic electro-catalytic activity for H_2O_2 reduction with low limit of detection ~ 60 nM at S/N = 3. Fluorescence of MCPs provides an optic feature which is also applied here for the detection of H_2O_2. The fluorescence quenching of MCPs@GNR can be achieved by addition of H_2O_2 which shows linearity over a range of increasing concentration of 10 μM to 150 μM.

*Author to whom correspondence should be addressed; E mail: drsanjeevkujjain@gmail.com; ksanjev@iitk.ac.in, Tel: + 91-512-2597968

1. INTRODUCTION

Hydrogen peroxide (H_2O_2) is a reactive oxygen species which is produced not only in chemical and industrial processes but also as a by-product of several oxidative metabolic pathways [1,2]. As it leads to oxidative damage in the living organisms resulting in cancer, hence its detection is practically important in biomedical, environmental and industrial research [3]. Prompted by this, researchers have been fabricating enormous enzyme based and enzymeless H_2O_2 sensors. However, usage of enzymes such as glucose oxidase (GO_x) [4], horseradish peroxidise (HRP) [5] provides high sensitivity; these sensors suffer from different practical limitations regarding loading concentration, pH and temperature [6]. This escorts the current research to turn to non-enzymatic electrochemical H_2O_2 detection which is mainly focused on transition metal oxide nanoparticles such as CuO [7], RuO_2 [8], Prussian blue (PB) [9], Fe_3O_4 [10], FeS/FeSe [11], TiO_2 [12] or redox polymers [13], carbon nanotubes [14] and graphene [15] based nano composites. In addition, novel metal nano clusters such as Ag [16] and Au [5] are used as fluorescence probe for H_2O_2 detection. Research articles discussed above involve either electrochemical detection or the fluorescence quenching methods. To the best of our knowledge, no report discussed an efficient sensor with dual traits of electrochemical and fluorescence sensing.

Another class of active materials include Coordination polymers (CPs), also known as metal-organic frameworks (MOFs), having metal ions linked by organic bridging ligands. They have been developed rapidly over the past few years for their potential applications as catalyst [17], contrast agents [18], light harvesting [19], drug delivery agent [20], encapsulating matrices [21], electronic and sensing devices [22-24]. Owing to their tunable pore size, optical and catalytic properties, CPs are vastly utilized in applications involving chemical sensing. Recently, Li et al. has successfully demonstrated that CPs can be used for

fluorescence enhanced nucleic acid detection and calorimetric detection of H_2O_2 and glucose [25]. Metalloporphyrins [26] and metallophthalocyanines [27] with excellent catalytic property and high chemical stability have been reported as efficient electrocatalytic H_2O_2 sensor. However, the major bottleneck to this high performance of the existing sensors is low conductivity, lesser active electrode surface and scarce charge carriers. An efficient strategy to overcome these limitations is to incorporate conducting material which not only enhance the surface area of the resulting composite but also facilitates charge transfer kinetics via network conductivity [28,29]. Among such conducting materials, graphene nanoribbon (GNR), a strip of graphene with a high length-to-width ratio, is a potential material owing to their high flexibility, large surface area, outstanding electrical conductivity with extended electrochemical stability and high optical transmittance [28-30]. In addition, graphene decorated with recognition species have already been in application to prepare chemical sensors and biosensors [31,32]. An amperometric sensor was fabricated by attaching picket-fence porphyrin on to graphene to sense chlorite ions [33]. Prussian blue nanoparticles on graphene act as an efficient sensor, for both, the reduction of H_2O_2 and oxidation of hydrazine [34]. Chen et al. have utilized maltose-grafted-aminopyrene modified graphene to detect lectinconcanavalin A by fluorescence quenching [35]. Highly sensitive ultraviolet sensor was also developed on a ZnO nanorod/graphene composite [36]. Moreover, Glucose oxidase (GOD) was bounded on graphene-Au nanoparticle hybrid to test sugar concentration in human serum samples [32]. Guo et al. have demonstrated enzymatic glucose detection on Pt-based CPs/graphene nanosheets [37] and Lu et al. [38] discussed the non-enzymatic glucose sensing by Ni(II) based CPs nanoparticle/graphene nanocomposite.

In this work, we have demonstrated that cobalt coordination polymer nanoparticles supported on graphene nanoribbons (MCPs@GNR), obtained through AOT isooctane/DMF

microemulsion-solvothermal synthesis, exhibits high electrocatalytic activity for H_2O_2 and its fluorescence quenches with increasing concentration of H_2O_2. Based on this, a non-enzymatic sensor has been successfully fabricated whose sensing ability is monitored by electrochemical as well as fluorescence quenching techniques.

2. EXPERIMENTAL SECTION

2.1 Materials and Methods

Glyoxal (40% aqueous), methanol, isopropyl alcohol, acetone, ethanol, isooctane, dimethyl formamide, *p*-phenylenediamine, carbon disulphide, phosphoric acid, sulphuric acid, potassium permanganate, 30% hydrogen peroxide, sodium hydroxide, potassium ferrocyanide/ferricyanide $[Fe(CN)_6]^{3-/4-}$ and cobalt chloride ($CoCl_2.6H_2O$) were purchased from Merck. Phosphate buffer solution (PBS) was purchased from s.d. fine-chemicals limited. MWCNT used for synthesizing graphene oxide nanoribbon was procured from Shenzhen Nanotech Port, Co. Limited, China. Perfluorinated ion exchange resin (Nafion) and sodium sulphosuccinate (AOT) was purchased from Sigma-Aldrich.

X-ray photoelectron Spectrometer, Perkin Elmer model 1257 was employed to study different specimen present in sample. UV-1601 Shimadzu UV-Vis spectrophotometer was used for recording the UV-Vis spectra. Fluorescence was conducted using a Cary Eclipse Spectrofluorimeter (Varian optical spectroscopy instruments, Mulgrave, Victoria, Australia). Powder X-Ray Diffraction (XRD) measurements were performed on Bruker D8 Advance X-ray diffractometer. Renishaw inVia Raman microscope was used for analyzing powder samples. FTIR spectra in KBr pellet form were obtained via Perkin-Elmer FT-IR spectrum BX spectrometer. Surface area was analyzed by N_2 adsorption–desorption isotherms using Micromeritics ASAP-2020. High resolution transmission electron microscopy (HRTEM) was

conducted on Phillips Technai T-300 microscope. Surface morphology of MCPs@GNR thin film was studied using scanning electron microscopy (Tescan, Vega 3 SBH model). Electrochemical tests were performed with CHI 604D electrochemical analyzer. Electrochemical characterization of the MCPs@GNR nanocomposite was carried out in an electrochemical cell, having three electrodes: Pt as counter electrode, Ag/AgCl as reference electrode (SCE) and MCPs@GNR/ITO as the working electrode.

2.2 Synthesis of graphene nanoribbon cobalt coordination polymer hybrids (MCPs@GNR)

Graphene oxide nanoribbons (GONR) was synthesized by longitudinal unzipping of carbon nanotubes as has been described in our earlier articles [28,39]. Synthesized GONR was used as support matrix for growth of cobalt coordination polymer nanoparticles (MCPs) using microemulsion-solvothermal process. Dithiocarbamate ligand (dtc-SB) having molecular formula $C_{16}H_{12}N_4Na_2S_4$ has been used for synthesizing MCPs and was prepared in two steps as described previously [40]. Here, we have used the anionic surfactant sodium sulfosuccinate (commonly known as AOT), to form reverse micelles which act as "reactors" for performing reactions leading to nanoparticles formation. AOT when dissolved in organic solvent (DMF) form thermodynamically stable spherical aggregates having hydrophilic head groups inside and hydrophobic tails extend into a nonpolar medium (isooctane). These reverse micelles having nanometer-sized DMF pools stabilized by surfactants served as reactor for the growth of MCPs nanoparticles on reduced GONR (i.e.GNR) surface [41]. In typical synthesis, 6g AOT was dissolved in 60 mL isooctane and was stirred for 2 hr. After stirring, it was divided into three parts having 20 ml each and named A, B and C. In part A and part B, 20 ml of 1 mmol $CoCl_2 \cdot 6H_2O$ and 20 ml 1 mmol of dtc-SB ligand in DMF solution were added. In part C, 20 wt% of GONR in DMF solution was added. All the three

reaction mixtures were then continuously stirred. Part B was then added dropwise to the part C and the reaction mixture was vigorously stirred for 30 min. After that, part A was added to the reaction mixture and stirred for another 30 min. The reaction mixture was then transferred to a stainless steel autoclave with Teflon lining and maintained at 100 °C for 24 hrs in a PID controlled oven followed by cooling to room temperature naturally resulting in black precipitate. As obtained product was centrifuged and washed with distilled water and absolute ethanol for three times. The final product (MCPs@GNR) was dried at 40 ^{o}C and kept in vacuum desiccator over night for further characterization.

2.3 Synthesis of Graphene nanoribbon

Graphene nanoribbon or reduced graphene oxide nanoribbon (GNR) are produced by reduction of GONR with hydrazine hydrate as described in our previous report [39]. GONR (110 mg) was ultrasonically dispersed in 30 ml DI water. Resulting uniform suspension was heated to 95 ^{o}C in an oil bath and 3 ml hydrazine hydrate was added slowly. The reduction was continued for 12 hrs and black precipitate was collected by filtration and washed with DI water and IPA several times before drying overnight in vacuum desiccator.

2.4 Fabrication of MCPs@GNR/ITO electrode

Finely grounded MCPs@GNR powder sample (10 mg) was taken in 5 wt. % Nafion solution in isopropyl alcohol and mixed ultrasonically for 30 min. Obtained suspension was sprayed on 1 cm^2 of "indium tin oxide" (ITO) plates using a spray gun under nitrogen ambient. These spray deposited thin films were dried at 60 ^{o}C overnight and used as working/electrochemical sensor electrodes.

3. RESULTS AND DISCUSSION

Figure 1a shows UV-Vis absorption spectra of GONR, GNR and MCPs@GNR nanohybrid dispersion in ethanol. The red-shifted π-π* absorption band of GNR at 276 nm compared to the band of GONR at 234 nm is consistent with the significant lowering of oxygen content and restoration of the π-π conjugated network [42] noted by recovery of electrical conductivity (I-V curve ESI S1). Similar red-shift is also apparent in MCPs@GNR where GNR act as scaffold. MCPs@GNR shows improved dispersion stability than GNR in most of polar solvents (Inset Figure). The solution dispersability of MCPs@GNR is studied using concentration dependence UV-Vis absorption spectroscopy. As can be seen from Figure 1b, absorption at 274 nm versus concentration curve follows a linear relationship (up to 33 mg/L) in ethanol indicating improved dispersion of MCPs@GNR [43]. Furthermore, emission bands at 428 nm for MCPs have shown negligible shift to 430 nm for MCPs@GNR (Figure 1c). Interestingly, the band intensity has shown small quenching on composite formation confirming efficient charge-transfer processes [43]. In contrast, the graphene nanoribbon emits no fluorescence.

Figure 2 shows the X-ray photoelectron spectra of C 1s, N 1s, O 1s, S 2p and Co 2p corresponding to GONR and MCPs@GNR nanocomposite. C 1s spectrum corresponding to GONR (Figure 2a) shows four different intensity peaks at 284.6, 285.9, 287.1 and 288.9 eV corresponding to the presence of sp^2 C-C/C-H, C-OH, C-O (epoxy) and C=O bonds respectively [44]. After nanocomposite formation, the peak intensity of C-O and C=O decrease significantly and the relative ratio of C-C/C-H shows increment (Figure 2b) as a consequence of restoration of conjugated sp^2 carbons and introduction of MCPs molecular structure [31]. Figure 2c shows N 1s XPS spectra having two peaks corresponding to two chemically inequivalent nitrogen atoms in MCPs molecular structure. Peaks at 400.4 eV and

398.3 eV signify pyrrolic nitrogen and pyridinic nitrogen [45]. Peak at 531.3 eV in O 1s spectra (Figure 2d) indicates the presence of Co-O-H in the structure which is consistent to literature [40,46]. Another peak at 532.9 eV in O 1s spectra shows correlation with the peak at 168.3 eV in S 2p XPS spectrum; which originates from oxidised sulphur [47] as shown in Figure 2e. This oxidised sulphur may arise by absorbed oxygen in MCPs. Peaks at 162.7 eV and 161.6 eV confirmed bridged sulphur and cobalt bound sulphur (Co-S-R) respectively. Furthermore, Co 2p spectra exhibits remarkable satellites along with binding energy difference (ΔE) of 15 eV between Co $2p_{1/2}$ and Co $2p_{3/2}$ (Figure 2f) [46].

FTIR spectra of GONR, MCPs and MCPs@GNR nanocomposite are shown in Figure 3a. Peaks of GONR are consistent with fingerprint groups such as carboxylic species (C=O, 1720 cm^{-1}), hydroxyl species (OH deformation, 1395 cm^{-1}; C-OH stretching, 1235 cm^{-1}) and epoxy species (C-O-C epoxy group stretching, 1060 cm^{-1}) [48]. Peak at 3300 cm^{-1} originate due to absorbed moisture. FTIR spectrum of MCPs is characterized by an anti-symmetric stretching vibration of CS_2 group at 1060 cm^{-1}, thioureide $S_2C{\cdots}N$ stretching vibration at 1390 cm^{-1} and 1603 cm^{-1} (C=N stretching) shows the presence of the dithiocarbamate and imine moiety in the structure [43,49]. N-H vibrations of MCPs shows two peaks at 3385cm^{-1} (antisymmetric stretching) and 646 cm^{-1} (rocking) [50]. The spectrum of MCPs@GNR largely resembles that of MCPs. The fingerprint carboxy and carbonyl peak (1720 cm^{-1}) vanishes completely and the peaks of other oxygen functionalities are diminished significantly indicating in-situ reduction of GONR during nanocomposite synthesis as has also been revealed by XPS spectra. The reduction of GONR and growth of MCPs nanoparticles are further confirmed by Raman and X-ray diffraction (XRD).

Figure 3b shows the comparative Raman spectra of GONR, MCPs and MCPs@GNR nanocomposite. GONR demonstrates the typical G and D bands at 1581 and 1370 cm^{-1}.

MCPs exhibits less intense peak at 670 cm^{-1} along with G band peak. After composite formation, it should be noted that the G and D bands in the MCPs@GNR are very similar to that of GONR. However, the MCPs@GNR spectrum shows a high intensity G band and a low intensity D band, which may be due to introduction of new sp^2 domains of highly conjugated MCPs nanoparticles as discussed in earlier sections. Moreover, the peak ratio of the G/D band is ~ 1.2, which is in good agreement with the previous reports for formation of few layer graphene nanoribbon structure [51]. High intensity broad 2D peak at 2685 cm^{-1} and a less intense peak at 670 cm^{-1} (green circle) can be ascribed to the growth of MCPs nanoparticles on few layered graphene nanoribbons [52].

Figure 3c illustrates XRD patterns of GONR, MCPs and MCPs@GNR. Diffraction peak at 10.04^o is assigned to GONR which corresponds to (002) plane, indicating the oxidation of MWCNT. The peaks corresponding to MCPs are located at 2θ = 18.54, 28.24, 28.97, 32.34, 33.66 and 48.48 which is indexed as (-141), (-232), (180), (-271), (-182) and (0132) planes (JCPDS pattern No. 053-1402). These characteristic peaks of MCPs are also observed in the XRD pattern of the composite MCPs@GNR, with the peaks of reduced graphene nanoribbon appeared at 26^o and 46^o. Interestingly, the peak at 46^o diminished significantly signifying the loading of MCPs on graphene nanoribbon. N_2 adsorption-desorption isotherm analysis of MCPs@GNR illustrated in Figure 3d exhibits high specific surface area (104 m^2g^{-1}) with H1 type hysteresis loop of Type IV isotherm.

Figure 4a shows the TEM image of graphene nanoribbon and inset demonstrates oxidative cleavage of MWCNT by chemical method. The chemical moiety attacks in axial direction of MWCNT, consequently resulting in layer by layer opening. Figure 4 b&c reveals that the MCPs nanoparticles mostly spherical in shape having dia ~6 nm are uniformly embedded on GNR surface. Enlarged image 4d clearly illustrates spherical MCPs

nanoparticle grown over GNR. Clear lattice fringes in HRTEM image (Figure 4e) represents that the lattice spacing of adjacent planes are 0.478 nm and 0.276 nm corresponding to (-141) and (-271) planes respectively. Two-dimensional fast fourier transform (2D-FFT) pattern computed from the MCPs section is shown in inset (Figure 4e). This also confirms the growth of MCPs particles in both (-141) and (-271) directions which are in correlation with SAED pattern in Figure 5a. Microstructure of the sample is further examined using scanning electron microscopy (SEM). Figure 5b show SEM micrograph of MCPs@GNR. It is noted that uniform sized nanospherical MCPs are distributed on wrinkled GNR. Inset image demonstrating enlarged view of MCPs nanosphere lying on GNR. From high magnification image (Figure 5c), under-lying MCPs nanospheres between layered GNR can be easily seen through nearly transparent GNR.

All these observations indicate that MCPs@GNR nanocomposite is synthesized with uniform distribution of MCPs nanospheres on the graphene nanoribbon. The possible formation mechanism of the MCPs@GNR nanocomposite under microemulsion-solvothermal condition can be explained as follows. As synthesized GONR and dtc ligand, both are π-rich structure; prior mixing of their individual microemulsion solution resulted in effective adsorption of dtc ligand onto GONR via strong π-π stacking interactions. Further, addition of cobalt ions led to formation of cobalt dithiocarbamate coordination polymer. The cobalt species present in resulting structure can further capture other ligand molecules in the solution by coordination interactions along different directions [53] resulting in metal coordination nanoparticles. In-situ reduction of GONR to GNR has taken place due to solvothermal treatment in DMF solvent. This reduction of GO, in which DMF served as both solvent and reductant have been reported earlier but the exact catalytic mechanism for this type of reduction is yet to be determined. However, the current state-of-art leads to

conclusion that the functional groups removal takes place by polarizing the carbon-oxygen bonds due to dipole-dipole interaction between DMF and GO functionalities [38,54-56]. It is worth noting that uniform size distribution of the MCPs is attributed to the presence of microemulsion reactors during growth process. The selective growth of MCPs nanoparticles on the surface of GNR is achieved via synergistic non-covalent charge transfer and π-π stacking interactions leading to the stabilization of the functionalized GNR. As a result of this non-covalent interaction, the chromophores in ligand do not lose their fluorescence and the MCPs@GNR nanocomposite remain fluorescent [43] as shown by Figure 1c. These MCPs nanospheres act as spacer and the aggregation of the graphene nanoribbon is prohibited. This makes both faces of GNR accessible resulting in high catalytic activity of the resulting composite [57]. The opening of MWCNT to form graphene oxide nanoribbon, growth of MCPs nanospheres along functionalities present on GONR and its H_2O_2 sensing activity is illustrated schematically in Figure 6.

Electrochemical behaviour of MCPs@GNR nanocomposite sensor

In order to understand the electron exchange features at electrode/electrolyte interface, the MCPs@GNR thin-film modified indium tin oxide (ITO) electrodes are firstly characterized by electrochemical impedance spectroscopy (EIS) in N_2 saturated 0.1 M phosphate buffer solution (PBS) (pH 6.6) with added mediator $[Fe(CN)_6]^{3-/4-}$ (10 mM) and NaCl (0.9 wt %). As can be seen from Figure 7a, MCPs modified ITO electrode exhibits large semicircle at high frequency with the charge transfer resistance, R_{ct} ~380 Ω suggesting that MCPs may play a blocking effect for ferricyanide/ferrocyanide redox couple and suppresses the rate of charge transfer due to its poor conductivity. In-situ reduced GONR results in formation of highly conducting nanocomposite with MCPs. Although GNR exhibits negligible R_{ct}, the semicircle decreases distinctively for MCPs@GNR modified electrode indicating that R_{ct} (40

Ω) for nanocomposite film is much lower than that of MCPs electrode. This phenomenon is further confirmed from the apparent diffusion coefficient (D_a) of ions estimated from the diffusion controlled regime ($\Delta Z_{im} / \Delta Z_{re} \approx 1$) which lies in the frequency range ~ 8 Hz to 0.8 Hz in the impedance data as discussed in our previous reports [39,58]. D_a across the MCPs@GNR/electrolyte interface is found to be 3.3×10^{-7} cm^2s^{-1} which is observed to be apparently 1.5 times higher than 2.08×10^{-7} cm^2s^{-1} for GNR electrode and ~14 times higher than 2.4×10^{-8} cm^2s^{-1} for MCPs electrode (Figure 7b). Higher D_a value for MCPs@GNR/electrolyte interface than GNR electrode may be attributed to the higher inter graphene sheet separation in MCPs@GNR compared to hydrazine hydrate reduced GNR, due to presence of the MCPs nanospheres at GNR surface. Consequently, ion diffusibility in vertical as well as horizontal direction is enhanced [59]. As a result of low R_{ct}, high conductivity and high diffusion coefficient, MCPs@GNR film has an accelerated electron transfer between the electrochemical probe $[Fe(CN)_6]^{3-/4-}$ and the electrode.

The consequent trend is reflected in the cyclic voltammetric responses. No sharp redox couples are observed for MCPs/ITO as well as GNR/ITO electrode in the working potential range 0-0.9 V (Figure 7c). Whereas MCPs@GNR/ITO shows a pair of stronger redox peak with high peak current (1:1) suggesting that the electron transfer is promoted by the MCPs@GNR nanocomposite [37]. The peak current measured for MCPs@GNR/ITO electrode are linearly proportional to the $[Fe(CN)_6]^{3-/4-}$ concentration (Figure 7d). CV shows optimal sensitivity for 10 mM $[Fe(CN)_6]^{3-/4-}$ (0.9 wt % NaCl) 0.1 M N_2 saturated PBS (pH 6.6). Under optimal condition, the effect of the scan rate on the electrochemical behaviours of MCPs@GNR/ITO electrode is investigated (Figure 7e). It is observed that both anodic peak (E_{pa}) and cathodic peak (E_{pc}) shift slightly to the positive and negative direction respectively. Peak currents, I_{pa} and I_{pc} are linearly proportional to the scan rate (Inset Figure

7e) with I_{pa}/I_{pc} ratio about unity in the range from 5 to 200 mVs^{-1} ($I_{pa}R^2$=0.9963; $I_{pc}R^2$=0.9976) reflecting surface-controlled reversible process [58].

The electrocatalytic activity of the MCPs@GNR nanocomposite is further studied for H_2O_2 redox reaction which is of great interest for biosensors. Based on above studies, the optimal solution used is N_2 saturated 0.1 M PBS (pH 6.6) with mediator $Fe(CN)_6]^{3-/4-}$ (10 mM) and 0.9 wt % NaCl. Figure 7f shows CV of MCPs@GNR/ITO sensor before and after injection of an aliquot of H_2O_2 at 60 mVs^{-1}. It is observed that, after addition of H_2O_2 the oxidation peak current at 0.5 V and the reduction peak current at 0.3 V at MCPs@GNR/ITO modified electrode shows enhancement. MCPs modified electrode as expected shows H_2O_2 redox response with very low measureable current (ESI Figure S2). In presence of Co (II) containing MCPs@GNR, the possible electrocatalytic oxidation and reduction mechanism of H_2O_2 at 0.5 and 0.3 V respectively can be summarized as in Eqs. [1] to [4]:

Oxidation

$$\text{Co (II) MCPs@GNR} \rightarrow \text{Co (III) MCPs@GNR} + e^- \quad [1]$$

$$\text{Co (III) MCPs@GNR} + 1/2\ H_2O_2 \rightarrow 1/2\ O_2 + H^+ + \text{Co (II) MCPs@GNR} \quad [2]$$

Reduction

$$\text{Co (II) MCPs@GNR} + e^- \rightarrow \text{Co (I) MCPs@GNR} \quad [3]$$

$$\text{Co (I) MCPs@GNR} + 1/2\ H_2O_2 + H^+ \rightarrow H_2O + \text{Co (II) MCPs@GNR} \quad [4]$$

Eqs. (1) to (4) are known mechanistic steps for oxidation and reduction of H_2O_2 at Co(II) modified electrode [27].

Furthermore, the electrocatalytic behaviour of MCPs@GNR sensor towards different concentrations of H_2O_2 is studied by amperometric response at 0.3 V. Figure 7g shows the amperometric current-time plot of the sensor upon the successive addition of the aliquots of H_2O_2 in PBS solution. When an aliquot of H_2O_2 is added into the stirred PBS, the current rises steeply to reach a stable value. The sensor accomplishes 98.4% of the steady state current in 3.6 s indicating fast amperometric response behaviour of the sensor. The inset corresponding to rectangular area in Figure 7g shows the low concentration current response of H_2O_2 and its calibration curve is shown in Figure 7h. The MCPs@GNR sensor exhibits two linear ranges, 20 μM to 15 mM with linear regression coefficient (R) of 0.9926 and 20 mM to 75 mM (R = 0.9990). The sensor exhibits high sensitivity of 1.73mA cm^{-2} mM^{-1} for lower concentration range and 0.16 mA cm^{-2} mM^{-1} for higher concentrations, which is better than most existing H_2O_2 sensors (Table 1) [31,60-68]. Limit of detection (LOD) is estimated to be 60 nM at signal-to-noise ratio 3. This enhanced sensitivity is attributed to the incorporation of graphene nanoribbon in the MCPs matrix. These facts suggest that the conducting support of graphene nanoribbon function as electron tunnelling centres resulting in improved sensitivity and response time by providing better electronic communications between catalytic centres.

Fluorescence response of the MCPs@GNR sensor towards H_2O_2

MCPs functionalized graphene nanoribbon (MCPs@GNR) designed for hydrogen peroxide detection possess dual functions including catalysis ability due to Co atoms and fluorescence as a result of ligand to metal charge transfer (LMCT) [40]. The black color colloidal suspension of MCPs@GNR in PBS emits intense fluorescence, $\lambda_{em.\ max}$ = 494 nm under UV light excitation of 365 nm. To test the potential of MCPs@GNR for detection of H_2O_2, the effects of temperature and PBS pH on the fluorescence intensity is investigated. We

examined the fluorescence of MCPs@GNR in the temperature range, 25 ^{o}C to 40 ^{o}C. Results reveal that the sensor performed best at 25 ^{o}C. Next, we tested the florescence intensities of MCPs@GNR in the absence and presence of H_2O_2 (10 μM) at various pH (ESI Figure S3) and the sensor demonstrates the optimal sensitivity at pH 7.4 (PBS 0.1M).

Under the optimal conditions, MCPs@GNR (0.1mg/mL) colloidal suspension in 0.1M PBS (pH 7.4) at 25 ^{o}C, various concentrations of H_2O_2 in solution is detected. As shown in Figure 8 a&b, the peak fluorescence intensity decreases linearly upon increasing the concentration of H_2O_2 over the range, 10 to 150 μM with LOD for H_2O_2 is 1 μM.

In order to have an insight in this H_2O_2 induced fluorescence quenching of MCPs@GNR, we observed the molecular structure of the MCPs. The MCPs is composed of cobalt ions coordinated with dithiocarbamate (dtc-SB) ligand [40]. In presence of H_2O_2, dithiocarbamates attached to cobalt ions are oxidized to form disulfides of dithiocarbamate. As a consequence, fewer dithiocarbamate ligands are bound to the metal ions, leading to reduced fluorescence [69,70].

Selectivity, stability and repeatability study

The effect of several possible interfering substances, such as ascorbic acid (AA), lactic acid (LA), uric acid (UA) and dopamine (DA) on the MCPs@GNR/ITO H_2O_2 sensor is investigated (ESI Figure S4). As can be observed, the addition of 0.05 mM of the above common interferents does not cause any observable change in the detection of H_2O_2. This insignificant interference effect on the electrocatalytic property demonstrates high selectivity of MCPs@GNR/ITO sensor towards the amperometric detection of H_2O_2 at 0.3 V vs SCE. The catalytic selectivity may be explained by the low working potential (0.3V) which permits the amperometric detection of only H_2O_2 at 0.3 V vs SCE, as interferents are active at higher

potential. The presence of Nafion (as a binder) cannot be neglected, as it is a perfluorinated anionic poly-electrolyte and possible interferents (AA, LA, UA, and DA) also exist in anionic form. Consequently, their presence could not interfere in the detection of H_2O_2 [62,71]. To determine the long-term stability, reproducibility and repeatability of the sensor system, MCPs@GNR sensor was studied over long period of time. It retained more than 90% of the initial response to H_2O_2 after 2 weeks storage. The reproducibility was estimated from the response of 1mM H_2O_2 at five MCPs@GNR modified electrodes prepared under identical conditions and a relative standard deviation (RSD) of 3.1% is acquired, indicating high stability and good reproducibility.

4. CONCLUSIONS

In summary, a facile approach based on in-situ reduction of graphene oxide nanoribbon during simultaneous growth of cobalt coordination polymer nanoparticles is utilized. This result in nanocomposite (MCPs@GNR) exhibiting dual function i.e. electrocatalysis and fluorescence for H_2O_2 sensing. MCPs@GNR modified electrode exhibits high electro-catalytic activity for H_2O_2 and the fabricated nonenzymatic H_2O_2 sensor, demonstrates wide linear range and low detection limit. The fluorescence of MCPs@GNR nanohybrid provides an optic feature which enables catalytic reaction of H_2O_2, resulting in the quenching of its fluorescence and is applied for H_2O_2 estimation. This study can be extended to other graphene nanoribbon/metal organic coordination polymer to generate dual functional nanohybrids by integrating the functions of MCPs and graphene nanoribbon via a simple one step synthesis.

ACKNOWLEDGMENTS

Authors thank USIC, DU for characterisation facility. S K Ujjain gratefully thanks DST INSPIRE fellowship program.

REFERENCES

(1) M. Ahmed, C. Pan, L. Gan, Z. Nawaz, J. Zhu, *J. Phys. Chem. C,* 2010, 114, 243-250.

(2) Z. Wen, S. Ci, J. Li, *J. Phys. Chem. C,* 2009, 113, 13482-13487.

(3) H. Ohshima, M. Tatemichi, T. Sawa, *Arch. Biochem. Biophys.* 2003, 417, 3-11.

(4) Y. C. Tsai, S. C. Li, J. M. Chen, *Langmuir,* 2005, 21, 3653-3658.

(5) F. Wen, Y. Dong, L. Feng, S. Wang, S. Zhang, X. Zhang, *Anal. Chem.* 2011, 83, 1193-1196.

(6) H. Teymourian, A. Salimi, S. Khezrian, *Biosen. Bioelectron.* 2013, 49, 1-8.

(7) M. J. Song, S. W. Hwang, D. Whanga, *Talanta*, 2010, 80, 1648-1652.

(8) M. Kang, Y. Lee, H. Jung, J. H. Shim, N. S. Lee, J. M. Baik, S. C. Lee, C. Lee, M. H. Kim, *Anal. Chem.,* 2012, 84, 9485-9491.

(9) K. S. Tsenga, L. C. Chena, K. C. Ho, *Sens. Actuators B,* 2005, 108, 738-745.

(10) X. Hu, J. C. Yu, J. Gong, Q. Li, G. Li, *Adv. Mater.,* 2007, 19, 2324-2329.

(11)A. K. Dutta, S.K. Maji, D. N. Srivastava, A. Mondal, P. Biswas, P. Paul, B. Adhikary, *ACS Appl. Mater. Interfaces,* 2012, 4, 1919-1927.

(12) L. C. Jiang, W. D. Zhang, *Electroanalysis,* 2009, 21, 988-993.

(13) H. C. Chen, M. Y. Hua, Y. C. Liu, H. W. Yangab, R. Y. Tsai, *J. Mater. Chem.,* 2012, 22, 13252-13259.

(14) M. Y. Hua, H. C. Chen, R. Y. Tsai, S. J. Tseng, S. C. Hu, C. D. Chiang, P. J. Chang, *J. Phys. Chem. C* 2011, *115*, 15182-15190.

(15) S. Guo, D. Wen, Y. Zhai, S. Dong, E. Wang, *ACS Nano,* 2010, 4, 3959-3968.

(16) T. Wen, F. Qu, N. B. Li, H. Q. Luo, *Anal. Chim. Acta,* 2012, 749, 56-62.

(17) K. H. Park, K. Jang, S. U. Son, D. A. Sweigart, *J. Am. Chem. Soc.,* 2006, 128, 8740-8741.

(18) K. M. L.Taylor, A. Jin, W. Lin, *Angew. Chem. Int. Ed.* 2008, 47, 7722-7725.

(19) Z. Zhang, K. Chen, K. P. Loh, *J. Am. Chem. Soc.,* 2009, 131, 7210-7211.

(20) W. J. Rieter, K. M. Pott, K. M. L. Taylor, W. B. Lin, *J. Am.Chem. Soc.,* 2008, 130, 11584-11585.

(21) R. Nishiyabu, C. Aime, R. Gondo, T. Noguchi, N. Kimizuka, *Angew. Chem. Int. Ed.* 2009, 48, 9465-9468.

(22) (a) E. Coronado, J. R.G. Mascaros, M. M. Capilla, J. G. Martinez, P. Pardo-Ibanez, *Adv. Mater.*, 2007, 19, 1359-1361. (b) I. Imaz, D. Maspoch, C. R. Blanco, P. M. J. Falcon, J. Campo, D. R. Molina, *Angew. Chem. Int. Ed.,* 2008, 47, 1857-1860.

(23) W. J. Rieter, K. M. L. Taylor, W. Lin, *J. Am. Chem. Soc.,* 2007, 129, 9852-9853.

(24) W. Cho, Y. J. Lee, H. J. Lee, M. Oh, *Chem. Commun.,* 2009, 4756-4758.

(25) (a) H. Li, X. Sun, *Chem. Commun*., 2011, 47, 2625-2627; (b) H. Li, L. Wang, Y. Zhang, J. Tian, X. Sun, *Macromol. Rapid Commun*., 2011, 32, 899-904.

(26) M. S. M. Quintino, H. Winnischofer, K. Araki, H. E. Toma, L. Angnes, *Analyst,* 2005, 130, 221-226.

(27) P. N. Mashazi, K. I. Ozoemena, T. Nyokong, *Electrochim. Acta,* 2006, 52, 177-186.

(28) S. K. Ujjain, P. Ahuja, R. K. Sharma, *J. Mater. Chem. A,* 2015, 3, 9925–9931.

(29) S. Stankovich, D. A. Dikin, G. H. B. Dommett, K. M. Kohlhaas, E. J. Zimney, E. A. Stach, R. D. Piner, S. T. Nguyen, R. S. Ruoff, *Nature,* 2006, 442, 282-286.

(30) J. S. Bunch, S. S. Verbridge, J. S. Alden, A. M. Van -der Zande, J. M. Parpia, H. G. Craighead, P. L. McEuen, *Nano Lett.,* 2008, 8, 2458-2462.

(31) S. Liu, J. Tian, L. Wang, X. Sun, *Carbon,* 2011, 49, 3158-3164.

(32) Y. Chen, Y. Li, D. Sun, D. Tian, J. Zhang, J. J. Zhu, *J. Mater.Chem.,* 2011, 21, 7604-7611.

(33) W. Tu, J. Lei, S. Zhang, H. Ju, *Chem.-Eur. J.,* 2010, 16, 10771-10777.

(34) Y. Jiang, X. Zhang, C. Shan, S. Hua, Q. Zhang, X. Bai, L. Dan, L. Niu, *Talanta,* 2011, 85, 76-81.

(35) Q. Chen, W. Wei, J. M. Lin, *Biosens. Bioelectron.,* 2011, 26, 4497-4502.

(36) H. Chang, Z. Sun, K. Y. F. Ho, X. Tao, F. Yan, W. M. Kwok, Z. Zheng, *Nanoscale*, 2010, 3, 258-264.

(37) Y. Guo, Y. Han, S. Shuang, C. Dong, *J. Mater. Chem.,* 2012, 22, 13166-13173.

(38) W. Lu, X. Qin, A. M. Asiri, A. O. Al-Youbi, X. Sun, *Analyst* 2013, 138, 429-433.

(39) P. Ahuja, V. Sahu, S. K. Ujjain, R. K. Sharma, G. Singh, *Electrochim. Acta,* 2014, 146, 429-436.

(40) S. K. Ujjain, P. Ahuja, R. K. Sharma, G. Singh, *Int. J. Chem.,* 2015, 7, 69-82.

(41) J. P. Cason, C. B. Roberts, *J. Phys. Chem. B*, 2000, 104, 1217-1221.

(42) D. V. Kosynkin, A. L. Higginbotham, A. Sinitskii, J. R. Lomeda, A. Dimiev, B. K. Price, J. M. Tour, *Nature,* 2009, 458, 872-877.

(43) A. Ghosh, K. V. Rao, S. J. George, C. N. R. Rao, *Chem. Eur. J.,* 2010, 16, 2700-2704.

(44) S. Gilje, S. Han, M. Wang, K. L. Wang, R. B. A. Kaner, *Nano Lett.,* 2007, 7, 3394-3398.

(45) S. A. Wohlgemuth, R. J. White, M. G. Willinger, M. M. Titirici, M. Antonietti, *Green Chem.,* 2012, 14, 1515-1523.

(46) (a) D. Atzei, A. Rossi, C. Sadun, *Spectrochimica Acta Part A,* 2000, 56, 1875-1886. (b) H. Baba, M. Nakano, *Inorg. Chim. Commun.,* 2012, 17, 177-179.

(47) D. Q. Yang, Y. Sun, Y. Guo, D. A. Da, *Appl. Surf. Sci.,* 1999, 148, 196-204.

(48) M. Jahan, Q. Bao, J. X. Yang, K. P. Loh, *J. Am.Chem. Soc.,* 2010, 132, 14487-14495.

(49) J. Gaur, S. Jain, R. Bhatia, A. Lal, N. K. Kaushik, *J. Therm. Anal. Calorim.,* 2013, 112, 1137-1143.

(50) D. L. Pavia, G. L. Lampman, G. S. Kriz, J. R. Vyvyan, Cengage Learning, 2007, pp. 22-92.

(51) T. Shimizu, J. Haruyama, D. C. Marcano, D. V. Kosinkin, J. M. Tour, K. Hirosea, K. Suenaga, *Nat. Nanotech.,* 2011, 6, 45-50.

(52) A. C. Ferrari, J. C. Meyer, V. Scardaci, C. Casiraghi, M. Lazzeri, F. Mauri, S. Piscanec, D. Jiang, K. S. Novoselov, S. Roth, A. K. Geim, *Phys. Rev. Lett.,* 2006, 97, 187401-187404.

(53) N. Girouda, S. Dorgea, G. Trouve, *J. Hazard Mater.,* 2010, 184, 6-15.

(54) Y. Chen, X. Zhang, P. Yu, Y. Ma, *Chem. Commun,.* 2009, 4527-4529.

(55) Z. Lin, Y. Yao, Z. Li, Y. Liu, Z. Li, C. –P. Wong, *J. Phys. Chem. C*, 2010, 114, 14819-14825.

(56) T. Kuila, A. K. Mishra, P. Khanra, N. H. Kim, J. H. Lee, *Nanoscale*, 2013, 5, 52-71.

(57) Y. C. Si, E. T. Samulski, *Chem. Mater.*, 2008, 20, 6792-6797.

(58) S. K. Ujjain, A. Das, G. Srivastava, P. Ahuja, M. Roy, A. Arya, K. Bhargava, N. Sethy, S. K. Singh, R. K. Sharma, M. Das, *Biointerphases,* 2014, 9, 031011 (1-11).

(59) V. Sahu, S. Shekhar, R. K. Sharma, G. Singh, *ACS Appl. Mater. Interfaces*, 2015, DOI: 10.1021/am5071706.

(60) W. Jia, M. Guo, Z. Zheng, T. Yu, E. G. Rodriguez, Y. Wang, Y. Lei, *J. Electroanal. Chem.*, 2009, 625, 27–32.

(61) S. Hanaoka, J.-M. Lin, M. Yamada, *Anal. Chim. Acta*, 2001, 426, 57–64.

(62) A. A.Ensafi, M. Jafari–Asl, B.Rezaei, *Talanta*, 2013, 103, 322–329.

(63) K. K. Lee, P. Y. Loh, C. H. Sow, W. S. Chin, *Biosens. Bioelectron.,* 2013, 39, 255–260.

(64) G. Wang, D. Cao, C. Yin,Y. Gao, J. Yin, L. Cheng, *Chem. Mater.*, 2009, 21, 5112–5118.

(65) H. Pang, F. Gao, Q. Chen, R. Liu, Q. Lu, *Dalton Trans.*, 2012, 41, 5862-5868.

(66) Y. Fan, N. Zhang, L. Zhang, H. Shao, Z. J. Wang, J. Zhang, C. Cao, *J. Electrochem. Soc.*, 2013, 160, F218-F223.

(67) Y. Fan, H. Shao, J. Wang, L. Liu, J. Zhang, C. Cao, *Chem. Commun.*, 2011, 47, 3469–3471.

(68) Y. Li, B. Tan, Y. Wu, *J. Am. Chem. Soc.*, 2006, 128, 14258-14259.

(69) Y. –C. Shiang, C. –C. Huang, H. –T. Chang, *Chem. Commun.,* 2009, 3437–3439.

(70) C. S. I. Nobel, D. H. Burgess, B. Zhivotovsky, M. J. Burkitt, S. Orrenius, A. F. G. Slater, *Chem. Res. Toxicol.* 1997, 10, 636-643.

(71) J. S. Narayanan, C. Anjalideva, V. Dharuman, *J solid state electrochem*, 2013, 17, 937-947.

List of Table

Table 1 Comparison of electrocatalytic activity of various modified electrodes towards H_2O_2 reduction.

Figure captions

Figure 1 (a) UV-Vis absorption spectra of GONR, GNR and MCPs@GNR in ethanol. Inset image shows comparison between dispersed solution stability of GNR (a) and MCPs@GNR (b) in ethanol after a week. (b) Concentration dependence of UV-Vis absorption spectra of MCPs@GNR in ethanol with increasing concentration from 3 mg L^{-1} to 33 mg L^{-1} (from a-k respectively). The inset shows the plot of optical absorption at 274 nm versus concentration. The straight line is linear least square fit to the data, indicating MCPs@GNR was dissolved homogeneously in ethanol. (c) Fluorescence spectra of MCPs, GNR and MCPs@GNR in ethanol, λex = 365 nm, λem= 428 & 430 nm respectively, slit width (5 nm/5 nm , 500 V PMT).

Figure 2 (a) C 1s XPS spectrum of GONR. (b) C 1s, (c) N 1s, (d) O 1s, (e) S 2p and (f) Co 2p spectra of the MCPs@GNR nanocomposite.

Figure 3 (a) FTIR spectra of GONR, MCPs and MCPs@GNR nanocomposite. (b) Raman spectra of GONR, MCPs and MCPs@GNR nanocomposite. (c) XRD spectra of GONR, MCPs and MCPs@GNR and (d) N_2 adsorption-desorption isotherm of MCPs@GNR.

Figure 4 (a) TEM image of GNR. Inset shows semi-opened MWCNT. (b) & (c) demonstrate MCPs@GNR nanocomposite. (d) Enlarged image shows MCP grown on GNR surface and (e) HRTEM image of MCPs@GNR nanocomposite where lattice fringes are clearly demarcated. Inset shows their two-dimensional Fast Fourier transform (2D-FFT) calculated from panel. FFTs are marked by yellow circle for clarity.

Figure 5 (a) SAED analysis. (b) SEM image of MCPs@GNR, Inset showing single MCPs nanosphere & (c) High magnification SEM images of MCPs@GNR nanocomposite, circular region showing MCPs nanospheres lying between layers of GNR.

Figure 6 Schematic illustrating nanocomposite formation and its sensing activity.

Figure 7 (a) EIS plot of MCPs (black), GNR (blue) and MCPs@GNR nanocomposite (red) in 0.1 M PBS (pH 6.6) having 10 mM $[Fe(CN)_6]^{3-/4-}$ and 0.9 wt% NaCl. (b) Plot of $|Z|$ vs $\omega^{-1/2}$ from impedance data for MCPs, GNR and MCPs@GNR nanocomposite. (c) CVs of MCPs, GNR and MCPs@GNR nanocomposite at 100 mV/s. (d) CV of MCPs@GNR in (0.1 M) PBS (pH 6.6) containing 0.9 wt% NaCl with three different concentrations (2 mM, 5 mM and 10 mM) of $[Fe(CN)_6]^{3-/4-}$. Redox peak currents have shown increment with increasing concentration of $[Fe(CN)_6]^{3-/4-}$ showing best performance with 10 mM solution. (e) CV of MCPs@GNR in (0.1 M) PBS (pH 6.6) containing 10 mM $[Fe(CN)_6]^{3-/4-}$ and 0.9 wt% NaCl at different scan rates. Inset figure shows variation of current versus scan rate. (f) CV of MCPs@GNR at 60 mV/s in absence and presence of 1.0 mM H_2O_2. (g) Amperometric current response of MCPs@GNR electrode upon successive injection of different concentrations of H_2O_2 into N_2 saturated 0.1 M PBS at 0.3 V. Inset shows enlarged view of lower concentration range and (h) Calibration curve with increasing molar concentration of H_2O_2 (0 mM to 100 mM) for MCPs@GNR sensor.

Figure 8 (a) Fluorescence response of MCPs@GNR nanocomposite after the addition of H_2O_2 (0-150 μM). (b) Calibration curve of Relative fluorescence emission with increasing molar concentration of H_2O_2.

Electrode modifier (electrode)	Transducer	Linear Range (L^{-1})	Detection limit (mol L^{-1})	Applied potential (V vs. Ag/AgCl)	Reference
CoTRP and cobalt oxide	Electrochemical	5.0×10^{-7}-2.0×10^{-3} M	2.0×10^{-7}	0.3 V	(26)
vertically aligned Co_3O_4	Electrochemical	0.0-5.35 0.0-1.4 mM	10 2.8	- 0.2 V +0.8 V	(60)
Co(II)-monoethanolamine complex immobilized on Dowex-50W resin	Chemi-luminescence	2×10^{-7}-2×10^{-5} M	1×10^{-7}	---	(61)
Nafion/exfoliated graphene oxide/Co_3O_4	Electrochemical	1.0μM-5.0 mM	0.3×10^{-6}	0.76 V	(62)
CoOOH nanosheets	Electrochemical	0.0-1.6 mM	40×10^{-6}	0.10 V	(63)
CoTCAPc-Au-ME SAM	Electrochemical	0.5–5.0 μM	0.4×10^{-6}	-0.2V	(27)
Ni foam supported-Co_3O_4 nanowire	Electrochemical	--	--	-0.4 V	(64)
Dendrite-like Co_3O_4 nanostructure	Electrochemical	0.0-1.7 mM	---	−0.77 V	(65)
Co_3O_4 nanosheets	Electrochemical	0.0-1.8 mM	1×10^{-6}		(66)
Co_3O_4 nanosheets	Electrochemical	0.0-~3.0 mM	--	−0.15 V	(67)
Co_3O_4 Nanowire	Electrochemical	0.0-~5.0 mM	--	−0.15 V	(68)
MCPs@GNR	Electrochemical & Fluorescence	20 μM- 75 mM 10-150 μM	60×10^{-9} 1×10^{-6}	0.3 V	This work

Table 1

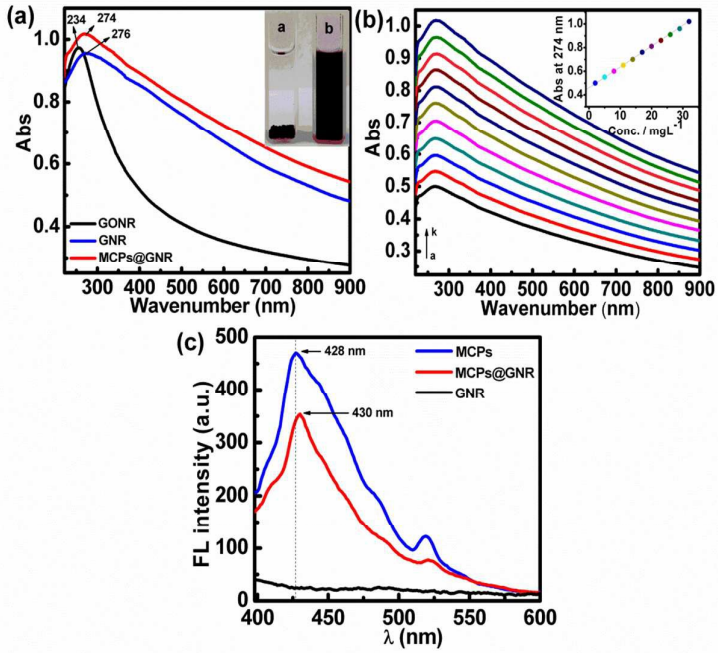

Figure 1

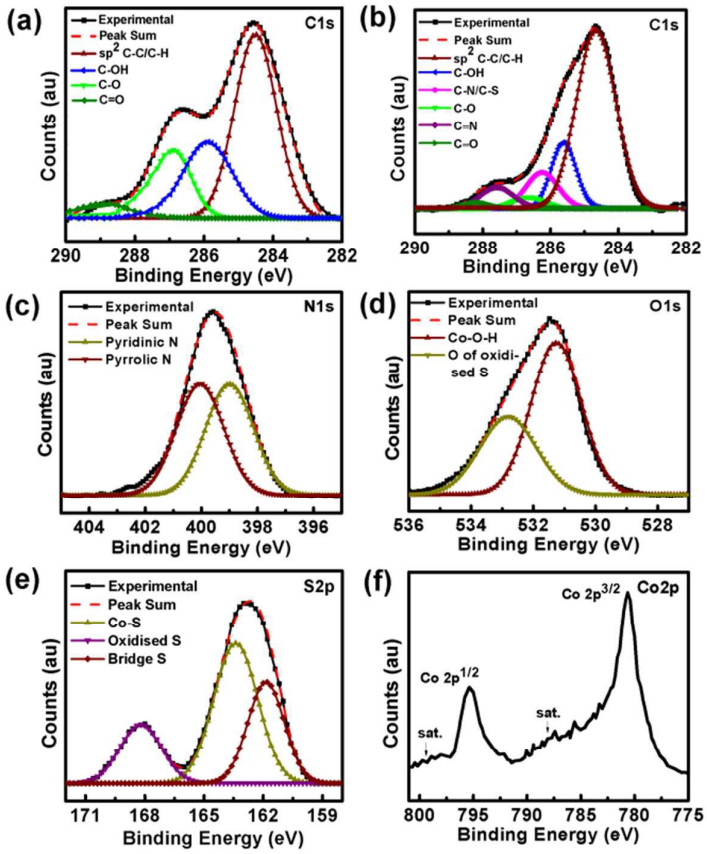

Figure 2

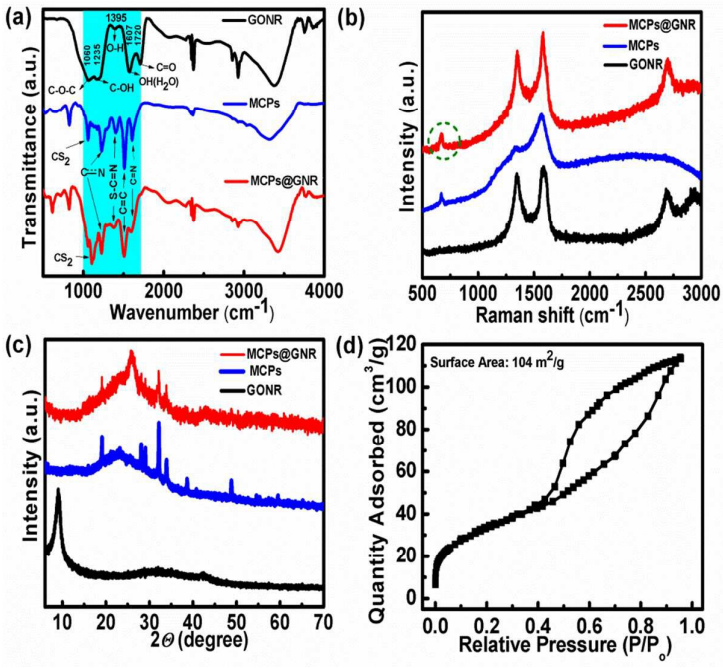

Figure 3

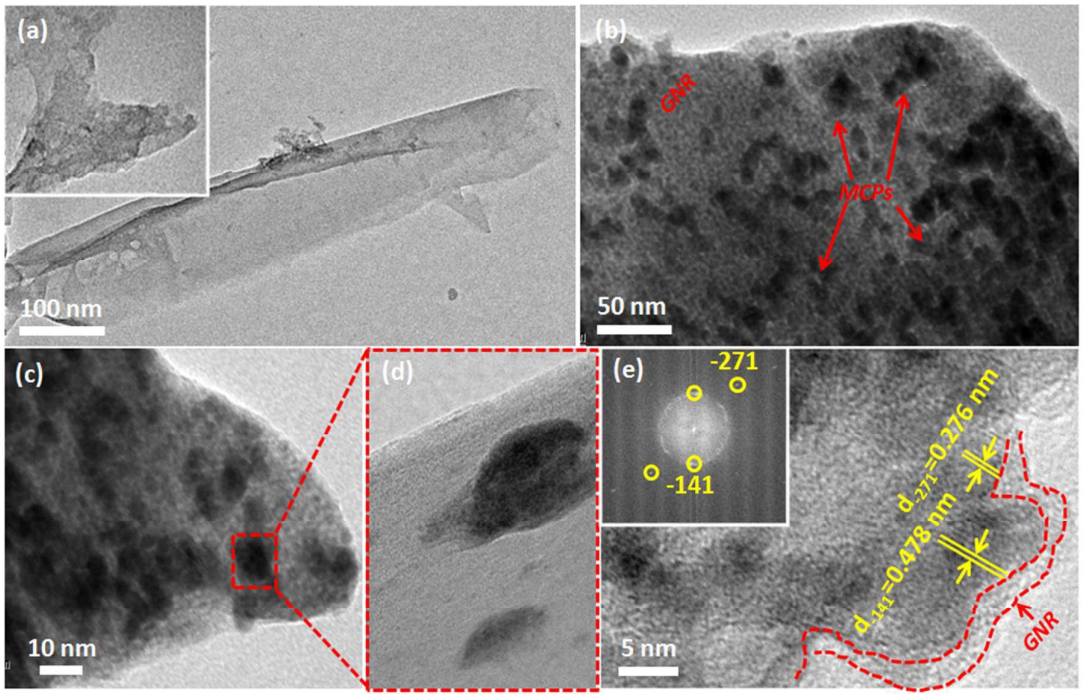

Figure 4

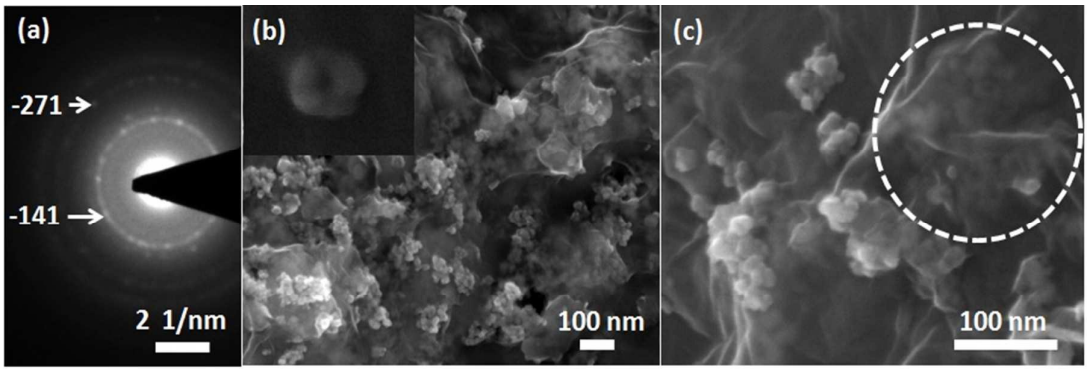

Figure 5

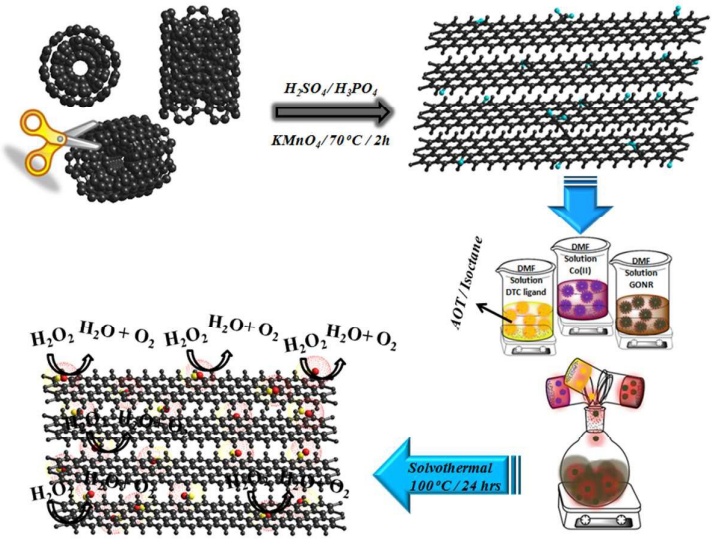

Figure 6

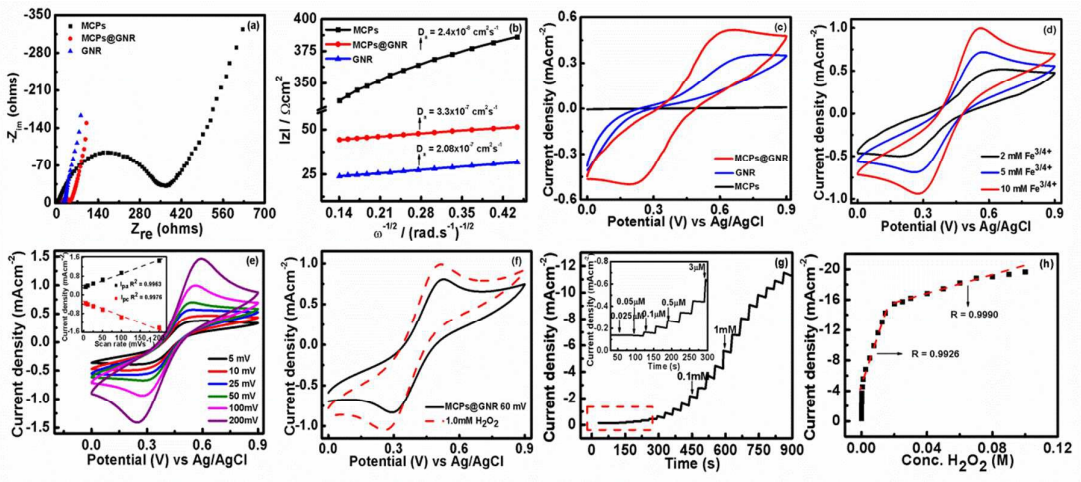

Figure 7

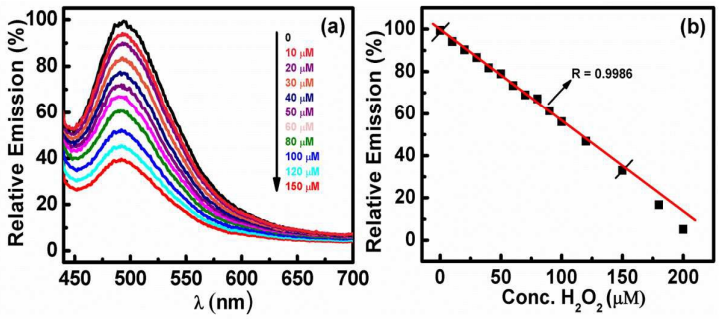

Figure 8